PCCP

Redox exfoliated NbS2: characterization, stability, and oxidation

Journal:	*Physical Chemistry Chemical Physics*
Manuscript ID	CP-ART-11-2022-005197.R1
Article Type:	Paper
Date Submitted by the Author:	23-Feb-2023
Complete List of Authors:	Nagaoka, Danilo; Mackenzie Presbyterian University, MackGraphe; Mackenzie Presbyterian University, School of engineering Grasseschi, Daniel; Federal University of Rio de Janeiro, Inorganic Chemistry ; UFRJ, Instituto de Química Cadore, Alisson; CNPEM, LNNano; Mackenzie Presbyterian University, MackGraphe Fonsaca, Jessica; Mackenzie Presbyterian University, MackGraphe Jawaid, Ali M.; Air Force Research Laboratory, Materials and Manufactoring Directorate Vaia, Richard A.; Air Force Research Laboratory, Materials and Manufactoring Directorate de Matos, Christiano; Mackenzie Presbyterian University, MackGraphe

ARTICLE

Redox exfoliated NbS_2: characterization, stability, and oxidation

Danilo A. Nagaoka[a,b], Daniel Grasseschi[c], Alisson R. Cadore[a], Jessica E. S. Fonsaca[a,b], Ali M. Jawaid[d], Richard A. Vaia[d], Christiano J. S. de Matos[a,b*]

Received 00th January 20xx,
Accepted 00th January 20xx

DOI: 10.1039/x0xx00000x

Niobium disulfide is a layered transition metal dichalcogenide which has just begun to be exploited as a two-dimensional material. Although it is a superconductor at low-temperatures and demonstrates great potential to be applied as catalyst or co-catalyst for hydrogen evolution reaction, only few reports demonstrated the synthesis of few-layer NbS_2. However, before applications can be pursued, it is essential to understand the main characteristics of the obtained material and its stability under atmospheric environment. In this work, we conducted a thorough characterization of redox exfoliated NbS_2 nanoflakes regarding their structure and stability in oxygen-rich environment. Structural, morphological and spectroscopic characterization demonstrated different fingerprints associated with distinct oxidation processes. This led us to identify oxide-species and analyse the stability of the redox exfoliated NbS_2 nanosheets in air, suggesting the most likely reaction pathways during the NbS_2 interaction with oxygen, which agrees with our density-functional theory results. The mastery over stability of layered materials is of paramount importance to target future applications, mainly because the electronic properties of these materials are strongly affected by an oxidizing environment.

1. Introduction

Transition metal dichalcogenide (TMD) crystals are known to be formed by elements from different groups and families.[1–3] In this scenario, niobium disulfide (NbS_2), a group-V TMD has first emerged as an exciting material due to its superconductivity at low temperatures.[4] Recently, other works have demonstrated its potential in different areas (*e.g.,* electronics,[5,6] sensing[6] and catalysis[7,8]), when obtained as nanosheets down to the few (FL) or monolayer (ML) thicknesses. Due to its interesting electronic properties, NbS_2 is a promising candidate to improve catalytic reactions, such as hydrodesulfurization and hydrogen evolution reaction (HER) activity,[9,10] with potential to replace the most efficient and expensive platinum catalysts. Other TMDs from group-VI (*e.g.,* MoS_2 and WS_2) with semiconducting properties have also been evaluated to play this role.[11] The main drawback of the latter, however, is the scarcity of reaction sites.[12] Group-V TMDs, on the other hand, possess a metallic character in its most stable phase,[13] and it has been shown that defects and imperfections cause specific rearrangements to their crystalline structure, which enhance adsorption/desorption events.[7,8] These sites are more reactive than the basal plane and favor the catalytic activity for, e.g., HER[10,11] Moreover, it was also recently demonstrated that their high conductivity improves ionic mobility, facilitating some catalytic reactions.[14]

Recently, Jawaid and co-workers reported the production of different TMD nanosheets, including NbS_2, through a redox exfoliation method, which is an alternative procedure to obtain mono-to-few layer TMDs.[15] Unlike most exfoliation methods via wet chemistry, the redox process takes advantage of in-situ chemical reactions. The reaction of mild oxidants with TMDs leads to the formation of peroxometalates, which further change into polyoxometalates (POMs). In view of their charge difference, POMs adsorb on the surface of the TMDs, react and subsequently exfoliate them.[16] In this scenario,[15–19] later works demonstrated the redox exfoliation viability in a variety of TMDs. Thereafter, this

[a] School of Engineering, Mackenzie Presbyterian University, São Paulo – 01302-907, Brazil
[b] MackGraphe, Mackenzie Presbyterian Institute, São Paulo – 01302-907, Brazil.
[c] Chemistry Institute, Federal University of Rio de Janeiro, Rio de Janeiro – 21941-909, Brazil.
[d] Materials and Manufacturing Directorate, Air Force Research Laboratories, Wright-Patterson AFB, Ohio 45433, United States

† * corresponding author: cjsdematos@mackenzie.br

Electronic Supplementary Information (ESI) available: [details of any supplementary information available should be included here]. See DOI: 10.1039/x0xx00000x

method is an attractive process for the scalable synthesis of TMDs due to its lowcost.[15] Furthermore, it stands out compared to other synthesis routes, considering the lack of strong reactants or the need for further treatments[20] (*i.e.,* annealing or purifications).

As new synthesis routes and applications emerge for NbS_2 nanosheets, it is imperative to comprehend fundamental issues regarding the material stability and the reaction pathways when exposed to different environments (*e.g.,* when dispersed or exposed to ambient conditions). To this end, we carried out a systematic study on redox exfoliated NbS_2 flakes to clarify the material's behavior under oxidation processes. Spectroscopic assessments were confronted with thermogravimetric analysis (TGA) and density functional theory (DFT) results regarding the susceptibility of NbS_2 to be oxidized and the reactions involved in this process. Also, a kinetic study conducted through UV-Vis spectroscopy led to a description of possible routes for the mono-to-few layer NbS_2 oxidation. The mastery over phase engineering and stability of novel layered materials is of paramount importance to target future applications. Thus, whenever seeking to verify the structure and integrity of reactive materials, understanding the mechanism in the involved reactions is undoubtedly essential.

2. Materials and Methods

The samples studied in this work were prepared following prior procedures.[18,21] In brief, 0.625 mmol (100 mg) of NbS_2 (Alfa-Aesar) was added to an argon filled 3-neck round bottom flask, followed by 5 mL of anhydrous acetonitrile (CH_3CN, Sigma-Aldrich). After equilibrating the temperature at 0°C (ice bath), 3 mmol of cumene hydroperoxide (562 µL of 80% CHP) was added dropwise to the NbS_2 suspension over the course of 15 minutes, and then the temperature was raised to 25°C to conduct the oxidation. After stirring for 24 hours, the sediment was collected. The redox step consisted of re-equilibrating the wet sediment to 0°C and adding a total of 125 µL of 0.010 M hydroquinone (Sigma-Aldrich) in CH_3CN in by aliquots over 2 hours. After 24h hours at 0°C, the solution was stirred for an additional 24 hours at 25°C. The mechanisms involved in the exfoliation process were thoroughly described in previous publications.[18,21] In summary, the mild oxidation, produced by CHP, charges the surface of the NbS_2 crystal, favoring interaction with *in-situ* produced polyoxometalates (POMs), which increases Coulombic repulsion and facilitates exfoliation. Finally, exfoliated flakes were collected by initially allowing the largest flakes to settle without stirring, centrifuging (10k RPM, 30 minutes) the collected supernatant, and redispersing the sediment in anhydrous solvent. Centrifugation and re-suspension were conducted 3-times. The top 2/3rds of the final supernatant contained few-to-monolayer NbS_2 flakes. X-ray diffraction (XRD), atomic force microscopy (AFM) and transmission electron microscopy (TEM) confirmed that the size distribution was similar to those in previous reports.[18,21] Also, x-ray photoelectron spectroscopy (XPS) was performed confirming oxidation after environment exposure.

Samples were analyzed under two different forms: (i) drop casted on different substrates and (ii) in a stable acetonitrile (ACN) suspension. The first sample, after drop casting onto SiO_2/Si substrates, naturally dried NbS_2 nanosheets were characterized by Raman spectroscopy, AFM, SEM, XRD and thermogravimetric analysis (TGA). To compare with the obtained redox exfoliated material, the bulk NbS_2 precursor was also mechanically exfoliated down to few layer NbS_2 using the scotch-tape method. Raman spectra were acquired using an Alpha300R confocal Raman spectrometer (Witec) with 532 nm excitation wavelength. For each spectrum, the integration time was set to 5 seconds with 10 accumulations. To control the sample exposure to the environment during the Raman analysis, nitrogen (N_2) gas purge was used to reduce the oxidation rate (except for when the oxidation was desired). To analyze the oxidation process in the drop casted material, the N_2 purge was turned off, and spectra were acquired with intervals of 5 minutes. To avoid thermally or optically induced degradation of samples a low laser power was used (500 µW) with 4 accumulations and 1 second integration time.

The AFM measurements on drop casted samples were taken using a Bruker Dimension Icon AFM in non-contact soft-tapping mode. Si substrates were prepared by UV-O treatment and drop-casting a dilute NbS_2 suspension (~1 mM) and drying under inert atmosphere. Average dimensions reflect ~100 flakes analyzed with the Nanoscope Analysis software. SEM images were obtained using a scanning electron microscope (JEOL-JSM 7800F) with 10 kV, secondary electrons were collected using a lower electron detector (LED). XRD measurements of the prepared samples drop casted on quartz substrates were carried out using a Rigaku Miniflex II system, with λCuKα radiation and a monochromator and slits with 30 kV and 15 mA. For the TGA measurements, flakes were drop casted directly and dried on the alumina cup kits (~1 mg) in an inert (Argon) atmosphere. The data were acquired using a TA Instruments TGA/DTA SDT Q600 system. A heat ramp of 5 °C/min was used, up to 1000 °C, in synthetic air environment.

NbS_2 samples were also studied directly in ACN suspension, being characterized by means of UV-Vis spectroscopy. The UV-Vis measurements were carried out using a UV-3600i Plus (Shimadzu) spectrophotometer, in a low volume (0.7 mL) quartz cuvette with a lid to avoid solvent loss through evaporation. To induce the oxidation of the otherwise protected NbS_2 flakes in the ACN suspension, an oxygen (O_2) purge (0.2 bar) was performed with a needle pinched through the cuvette lid. The NbS_2 flakes in the suspension were kept in the closed cuvette to avoid solvent evaporation during 1-minute O_2 purge cycles. UV-VIS spectra were then acquired between purge cycles, until the end of the reaction (*i.e.,* no detectable change in the spectra) was verified (which occurred after 15 minutes).

DFT calculations[22] were performed with the Quantum Espresso 6.4.1 simulation package using a plane-wave basis set with an energy cutoff of 400 eV.[23,24] Precision standard solid-state pseudopotentials (SSSP) were used for all atoms.[24,25] The generalized gradient approximation described the exchange-correlation functional with Perdew-Burke-Ernzerhof (PBE) parameterization, considering 12 points K (x,y). [22] We first modelled ML-NbS_2 and ML-NbO_2, using hexagonal unit cells and periodic boundary conditions. A vacuum spacing of 20 Å was added to avoid interaction between the periodic layers. Structural optimization was performed with force tolerance of 10^{-5} eV/Å. Phonon modes were calculated using the equilibrium structure from the self-consistent calculation. The phonon frequencies were calculated by diagonalization for the dynamical matrix. The intensities of each mode were obtained through the Placzek approximation.[26] All input files are in the Support Information. For modelling O_2 adsorption we used the Gaussian09 utilizing the same functional parametrization n previous describe above. A 4x4 supercell was constructed using the relaxed structure for NbS_2, and this structure was used as a finite cluster. Three different scenarios were analyzed, the O_2 adsorption on the basal plane (O_2@NbS_2-b), on the edge (O_2@NbS_2-e), and a sequential adsorption first on the edge and then on the basal plane ((O_2)$_2$@NbS_2).

3. Results and Discussion

Initial Characterization: drop casted samples

Images of the redox exfoliated NbS_2 nanosheets were obtained using SEM to verify the samples aspect after drop casting, these are shown in Figure S1. Lateral dimensions of the flakes ranged from 50-300+ nm. AFM height measurements were 2.1 nm +/- 0.5 nm, corresponding to 1-2 layers per flake with a distribution up to 5-6 layers (~7-9 nm). [15,18] The discrepancy between AFM measurements and crystallographic layer thickness is in line with deviations due to tip-surface interaction and surface-surface interactions, especially in atomically thin, two-dimensional materials.[27,28] Next, by using XRD diffractograms we were able to compare the exfoliated material and its bulk precursor as depicted in Figure S2, with clear differences between the samples. The peaks observed in the bulk sample confirm NbS_2's 3R phase (JCPDS: 03-065-3655). As expected, the well-defined and sharp peaks, present in the bulk NbS_2 sample, broaden or disappear indicating a decrease in the number of crystalline planes. However, it is interesting to note that the peak related to the interlayer stacking, (0 0 3) plane close to 14° degrees, is always present,

indicating the maintenance of the lamellar characteristic. Also, a small shift to lower angles can be seen in this peak for the exfoliated material, due the increase of distance between layers.

The Raman spectra of a representative redox exfoliated NbS_2 nanosheet (blue) and of a mechanically exfoliated flake (red) is presented in **Figure 1** together with a Raman spectrum of the bare substrate (dashed black). Overall, the acquired Raman spectra for the NbS_2 samples agree well with each other (indicating negligible impact to crystallinity by the chemical reactions involved in redox exfoliation) and with those in previously reported chemical vapor deposition (CVD) NbS_2.[5,8,14] Assuming that the crystals do not undergo phase changes during exfoliation, we use the 3R phase mode assignment for the FL samples.

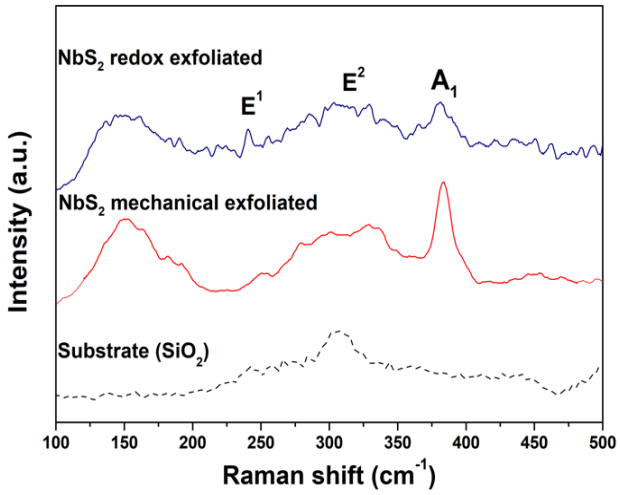

Figure 1. Raman spectra of mechanically (red) and redox (blue) exfoliated NbS_2 flakes. A spectrum of the bare substrate (SiO_2/Si) is also presented for comparison (dashed, black).

For simplicity, we call the modes by their bulk irreducible representation names (even for the FL samples). 3R NbS_2 (C_{3v}^5 space group) exhibits 4 active Raman modes: $2A^1$ + 2E. In **Figure 1**, we indicate the positions of E^1, E^2 and A_1 modes, according to previous literature assignments. Comparison between the mechanically and redox exfoliated samples shows that the former exhibits a more well-defined A_1 peak, which may be due to a better conservation of the crystal's basal plane[29,30]. The E_1 peak was found to vary from flake to flake in redox exfoliated flakes, possibly due to small structural and/or thickness variations. Note that this mode is also visible in the mechanically exfoliated sample, but with a smaller amplitude and with a larger Raman shift. The assignment of the band observed at around 150 cm^{-1} is still controversial in the literature. While Kitaura and colleagues relate it to a two-phonon scattering process,[31] Redwing and co-workers attribute this band to a defect mode in the 3R phase.[32]

Oxidation in drop casted samples

For studying oxidation in redox exfoliated NbS_2, individual flakes were monitored under the confocal Raman spectrometer for 4 hours with time intervals of 5 minutes. Selected Raman spectra for various exposure times are depicted in **Figure 2**. One can easily identify changes in the Raman spectra over the monitored time. Besides an overall intensity decrease of the NbS_2 Raman modes (not shown, as each spectrum was normalized by its highest peak), a change in their relative intensity as well as the appearance of new modes are noteworthy. In fact, in the last recorded spectrum (red/top solid line in **Figure 2**), the modes associated to the substrate (dashed/bottom curve) were more evident than those of the sample. The significant changes in the spectrum indicate the material's instability when exposed to ambient conditions (*i.e.*, O_2 and H_2O). While the initial spectrum is consistent with several reports in the literature for NbS_2 and is similar to the spectrum shown in Figure 1, after approximately 30 minutes of environmental exposure the shape of the identified peaks exhibit clear changes. Interestingly, after 200

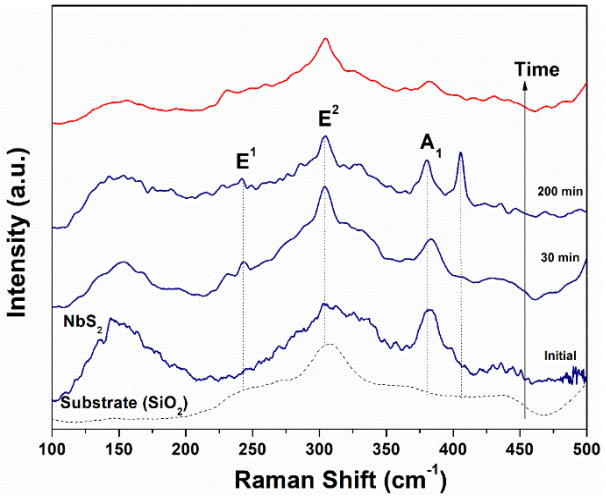

Figure 2. Selected Raman spectra of NbS_2 obtained at the indicated times during exposure to room environment. Dashed: Raman spectrum of the substrate; vertical dotted lines indicate the position of the assigned NbS_2 modes

minutes the appearance of a new peak close to 408 cm^{-1} is noticeable. It is important to emphasize that, even though a mode near 408 cm^{-1} has sometimes been reported and assigned to NbS_2[33,34] the fact that, in our case, it only emerges after some reaction time indicates possible association to oxidation. Also, it matches a mode observed in our simulations and associated to the first stage of niobium dioxide (NbO_2), as will be addressed ahead. In the last acquired spectrum, in red, the decrease in intensity of all Raman peaks associated with the sample is probably caused by amorphization of the crystal after reaction with the environment.

It is known that phase-transition of 2D materials might be prompted by a variety of factors[35] (*e.g.,* surface modification, high pressure, high temperature, etc.). As the changes in the spectrum are only observed in the redox exfoliated NbS_2 after environmental exposure, we postulate that they are triggered by oxidation processes, which up to this date has not been studied in detail for NbS_2 nanomaterials. A few studies[14,36] reported on the oxidation of CVD grown, non-stoichiometric, $Nb_{1+x}S_2$ samples. It is believed that non-stoichiometry increases the density of active sites on the basal plane, increasing reactivity.

Note that, in our experiments, the peaks that emerge over time are sometimes weak and/or transient. For better clarification we provided in Figure S8 the time dependent spectra evolution without any treatment. We attribute this to the fact that uncontrolled oxidation leads to an amorphous structure, with significant site-to-site structural and compositional variations. If this is the case thermal annealing would induce a more uniform crystallization. To further investigate this possibility, we carried out a thermal treatment on a drop casted NbS_2. For this purpose, a sample exposed to ambient environment for hundreds of minutes was annealed at 1000°C under an inert (Argon) environment for 15 minutes. Optical images of the sample before and after the thermal treatment are presented in Figure S3. From this figure, it is possible to see the modification of the sample's morphology, from a more uniform coverage of the substrate, Figure S3a, to two types of localized clusters of different sizes, Figures S3b and S3c.

Subsequently, we repeated the Raman characterization and **Figure 3** depicts the two types of Raman spectra observed in the final material. The smaller (Figure S3b) and larger clusters (Figure S3c) respectively yield the red and blue Raman spectra in **Figure 3**, respectively. Analysis demonstrates clear differences between these spectra and, even more apparent, from those observed in pristine (**Figure 1)** and naturally oxidizing (**Figure 2)** NbS_2 flakes. Comparison with the literature (as well as simulations to be show below) reveal that the spectra in **Figure 3** can be associated with two different niobium oxide (Nb_xO_y) species: NbO_2 (red) and Nb_2O_5 (blue). The spectrum in blue can be assigned to Nb_2O_5, since it presents a broad band centered at around 700 cm^{-1}, characteristic of the amorphous phase of Nb_2O_5.[36,37] The two bands at lower energies (139 cm^{-1} and 264 cm^{-1}) are related to vibrations of the distorted NbO_6 octahedral, which corresponds to the T-Nb_2O_5 phase[38] (orthorhombic). The spectrum shown in red, on the other hand, resembles the data available in the literature for NbO_2, with the characteristic bands at 140 cm^{-1}, 297 cm^{-1}, 407 cm^{-1}, 893 cm^{-1}, and 920 cm^{-1}.[37,39] It is interesting to notice that the appearance of a peak at 407 cm^{-1} for NbO_2 closely matches both a peak observed in the naturally oxidized sample (at 408 cm^{-1} for 200 minutes in **Figure 2**) and simulation data obtained (to be discussed below). These results are in line with the assumption that NbS_2 oxidizes to an amorphous stage

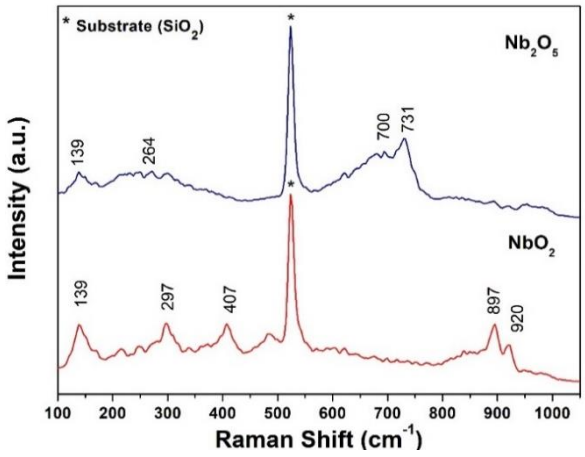

Figure 3. Representative Raman spectra (λ = 532 nm) of the annealed (1000°C for 15min in Argon) drop casted oxidized NbS_2 samples. The red line is related to the spectrum in a smaller NbO_2 cluster (Figure S3b), whereas the blue line to a larger cluster predominantly Nb_2O_5 (Figure S3c). Asterisks indicate modes associated with substrate.

that, after annealing, crystalizes into different niobium oxide species.

Next, seeking to evaluate the steps involving in the oxidation process, we further assess the behavior of our NbS_2 material under thermal treatment in an oxidizing medium by performing TGA analysis in a synthetic air-controlled atmosphere (see Methods for details). The weight loss percentage curve is depicted in **Figure 4**, along with differential thermal analysis (DTA). Figure S4 also presents the differential scanning calorimetry (DSC) results obtained. In **Figure 4** it is possible to identify different processes during the TGA measurements. The first one is related to the solvent evaporation, corresponding to approximately 1.44% in mass between 30-120°C. Subsequently, it is noticeable a gain of mass at 335°C, suggesting the incorporation of O_2 by the NbS_2, therefore generating an unstable compound. Shortly after that, there is a loss of sulfur dioxide (SO_2), approximately 2.7%, which takes place from 335°C to 450°C.[40,41] These two events indicate the formation of intermediate species, such as NbSO, corroborating the obtained DSC curve (Figure S4), which exhibits a wide exothermic event, in accordance with the solvent oxidation and loss, followed by an endothermic event at around 400°C. That is in line with adsorption processes, attesting O_2 incorporation in this step.[42,43] At higher temperatures (450°C to 600°C), a weight loss of 7% could be attributed to the complete removal of S and a stable oxide crystal formation. The residual mass (~80%) could be attributed both to Nb_2O_5, which should melt just at 1400°C,[42,44] and/or to NbO_2, which has a melting point of about 1900°C.[44] To verify this assumption, the resultant solid was taken to Raman analysis, and the obtained spectrum is depicted in Figure S5. The apparent similarities to spectra red and blue, previously discussed in **Figure 3,** attest that the final residue is possibly a mixture of NbO_2 and Nb_2O_5.

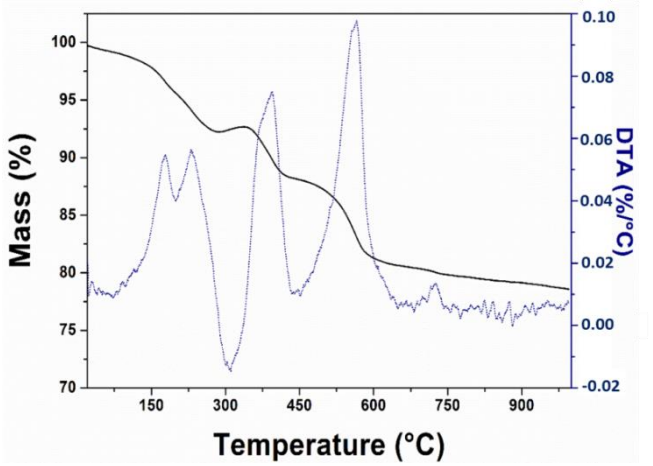

Figure 4. Thermogravimetric analysis (TGA) and differential thermal analysis (DTA) of mono-to-few layer NbS_2 (in air). The black line (TGA) demonstrates the different events of mass loss and gain along the temperature range. The blue dashed line is the first order.

So far, the presented results identify that redox exfoliated NbS_2 experiences oxidation under different conditions, undergoing pathways that may lead to distinct species (*i.e.,* Nb_2O_5, and NbO_2). The possible pathways, however, are vast and complex, and other species could also be involved (*e.g.*, NbO and NbSO), as discussed in our TGA analysis. Thus, to validate and understand our experimental results, we carried out ab initio simulations of ML-NbS_2 and verified how the adsorption of O_2 molecules take place on its surface. For this purpose, we used DFT, and the results will be discussed next.

Density Functional Theory study

The structures used to generate our simulated data are presented in **Figures 5a-b**, being relative to ML-NbS_2 and ML-NbO_2, respectively. Simulations initially considered periodic boundary conditions, so that an infinite monolayer plane was modelled. In both cases, simulations started with the P*6/mmc* space group[45] and the structures were allowed to relax. Although we also speculate indications of Nb_2O_5 formation in the final steps of NbS_2 oxidation, calculations could not be performed with this structure because of hardware limitations.

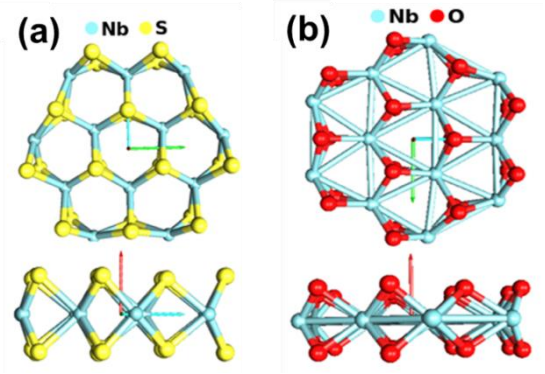

Figure 5. Relaxed crystalline structures obtained by DFT simulation in Quantum Espresso: (a) ML-NbS_2 and (b) ML-NbO_2. Top panels illustrate the top view, whereas the bottom panel depict the lateral view of the structures.

The electronic band dispersion and the projected density of states (PDOS) of the NbS_2 structure are presented in Figure S6. They agree with the results from[41,42], thus validating our data and allowing NbS_2 to be used as a starting material for further simulations. NbS_2 shows a metallic behavior with the valence band crossed by the Fermi level. The PDOS demonstrates the contribution of the *d* orbitals from Nb, implying that the electronic properties are mainly from the metallic atom (Nb). After identification of the optimized NbS_2 structure, we computed its active phonon modes at the *Γ* point. Our calculations demonstrated the existence of three Raman-active modes as shown in the Table 1. The comparison between the calculated NbS_2 phonon modes and the experimental Raman modes is also shown in Table 1.

Overall, the experimental and theoretical mode showed a good agreement, mainly for the E^2 and A_1 modes. Figure S7 shows the band dispersion and PDOS for the simulated NbO_2 structure, which exhibits a similar characteristic to that of NbS_2, with a half-filled valence band and a metallic characteristic. As in the NbS_2 analysis, Nb atoms have the highest contribution for the PDOS of the valence states. Our theoretical observations for the oxide are also in agreement with previous studies. [46,47] Next, we calculated the phonon modes at the *Γ* point for the optimized NbO_2 structure. Eight Raman-active modes were numerically observed, as shown in the Table 1. Five of these modes agree well with those shown by the red line in **Figure 3**, which corroborates our assumption that the small clusters obtained after annealing correspond to NbO_2 crystallites. The experimentally obtained frequencies are also shown in Table 1. Our theoretical model assumes a perfect crystal; therefore, slight numerical-experimental discrepancies are observed. Those can either reflect the polycrystallinity of NbO_2, or some imperfections in the crystal lattice. Otherwise, the Raman modes at 407 cm^{-1}, 483 cm^{-1}, 893 cm^{-1} and 922 cm^{-1} are in good agreement.[37,48] In summary, it is possible to compare the materials and establish a good match among our experimental and simulation study, as well as with previous reports.[37,45]

Table 1. Comparison between DFT simulated and experimental Raman modes.

NbS_2		**NbO_2**	
Theoretical	**Experimental**	**Theoretical**	**Experimental**
Frequency (cm^{-1})	**Frequency (cm^{-1})**	**Frequency (cm^{-1})**	**Frequency (cm^{-1})**
207	244	284	249
290	288	394	407
378	382	483	483
		565	-
		764	-
		800	-
		874	893

Next, to shed light onto the oxidation reaction dynamics, NbS_2 nanoflakes were numerically modelled (as the edges are known to be important active sites). We used a 4x4 supercell with zig-zag edges and calculated the adsorption energy (E_{ads}) of O_2 molecules onto the NbS_2 surface and edges. O_2 molecules were found to adsorb on Nb atoms, which is reasonable, considering the hard-soft acid-base characteristics of oxygen and sulfur, favoring the reaction with Nb. As mentioned before, three different scenarios were analyzed: O_2 adsorption on (i) the basal ML-NbS_2 plane (NbS_2@O_2-b); (ii) the ML-NbS_2 edges (NbS_2@O_2-e), and (iii) the basal ML-NbS_2 plane after oxygen adsorption to the edge (NbS_2@$(O_2)_2$). The results are expressed in **Figure 6**. The configuration

corresponding to isolated O_2 molecule and NbS_2 nanoflake (left-most) is taken to be the energy reference. The second left-most configuration is the result for $NbS_2@O_2$-b, with E_{ads} = 1.7 eV, indicating a non-spontaneous adsorption. In other words, energy is required so that it can occur, characterizing an endothermic process. On the other hand, for the third simulated configuration, $NbS_2@O_2$-e, E_{ads} = -1.45 eV, indicating a spontaneous and exothermic reaction. Indeed, it is expected that the material's edges or imperfections would be the preferred reaction site for interactions. The results agree well with our TGA results (**Figure 4**) that showed the incorporation of O_2 in the structure as the temperature rises through an endothermic event (Figure S4). Finally, we considered a fourth configuration, $NbS_2@(O_2)_2$, takes place after the first O_2 adsorption onto the edge, in which case we can see that E_{ads} for basal plane adsorption drops to -1.60 eV, indicating that the adsorption becomes spontaneous.

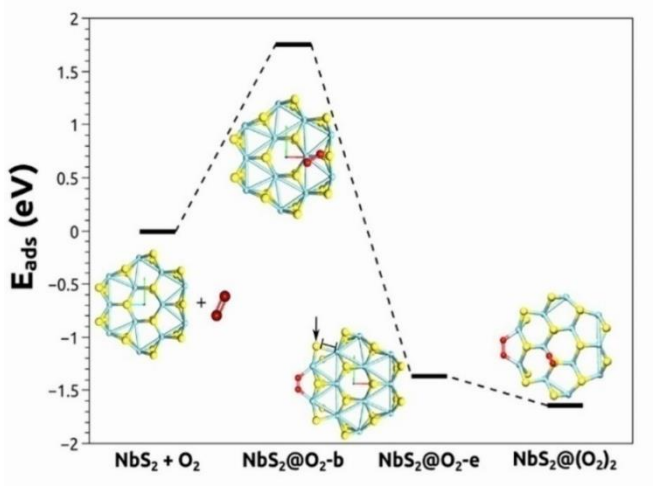

Figure 6. Adsorption energy (Eads) diagram of O_2 on nanosized ML-NbS_2. First configuration (left-most): pre-adsorption situation, used as the energy reference. Second configuration: adsorption of O_2 to the ML-NbS_2 basal plane, leading to a positive adsorption energy (non-spontaneous reaction). Third configuration: adsorption of O_2 to the ML-NbS_2 edge, leading to a negative adsorption energy (spontaneous reaction). Fourth configuration (right-most): adsorption to the basal plane after edge oxidation, in which case Eads is negative, demonstrating that the edge functionalization catalyses oxidation of the basal plane sulphur atoms can be replaced by the atmospheric O_2.

Therefore, our DFT simulations suggest that a mildly oxidizing environment could constrain the reaction to the edges. This phenomenon agrees with the redox exfoliation procedure once this process uses mild oxidant.[15,18] Thus, by controlling the chemical potential during the synthesis, the basal plane of the material is preserved. Additionally, these results reveal that the NbS_2 oxidation should be an autocatalytic process, where oxidating spots at the crystal's edges decrease the activation energy for the subsequent oxidation of the basal plane.

Oxidation in suspension: a kinetic study

Aiming at thoroughly tracking the oxidation process, we carried out a systematic study of the kinetics involved in the NbS_2 degradation under a controlled environment. More specifically, we induced the oxidation of otherwise stable NbS_2 suspensions in ACN and monitored it through UV-Vis analysis. **Figure 7a** presents the UV-Vis extinction spectra collected at different O_2 exposure times (see Methods for more details).

Initially, the redox exfoliated NbS_2 dispersion has a largely featureless spectrum (Figure 7a, black) that is typical of a metallic character, with extinction steadily increasing towards the UV. This trend might be related to different processes, such as photon absorption followed by nonradiative decay (*e.g.,* electron-electron scattering) or Rayleigh scattering.[49] Also, as demonstrated in our simulated data (Figure S7), the energy difference between the valence and conduction bands allows for the existence of interband transitions within the UV.[37,47]

As O_2 reacts with the dispersed NbS_2, a peak in the 225-260 nm region appears (marked by the square in Figure 7a) and a peak at around 278 nm (indicated by the diamond) stands out from the broadband extinction trend. In addition, the existing UV extinction seems to red shift, developing a peak at just above 200 nm (indicated by the asterisk). All these features can tentatively be attributed to the formation of Nb oxides, which would corroborate our previously discussed results. Based on the evolution of each peak over time, kinetic curves were prepared aiming at shedding more light onto NbS_2 oxidation and assign the specific rate constants (*k*) to each identified mechanistic stage. It is important to mention here that although the measured spectra express extinction, encompassing absorbance as well as scattering processes, for kinetic analysis we assumed the spectra to be dominated by absorbance

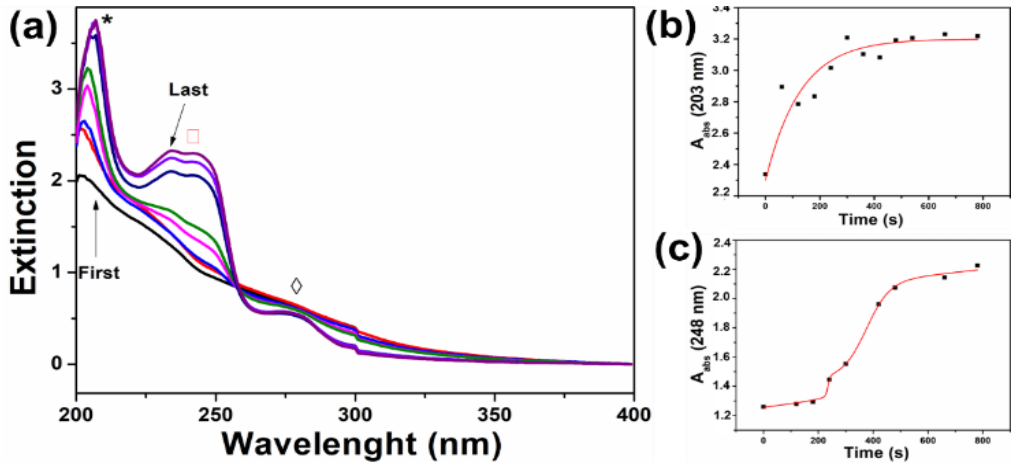

Figure 7. (a) UV-Vis spectra at different reaction times for NbS_2 oxidation. Kinetic profiles obtained by monitoring extinction (At) at (b) 203 nm and (c) 248 nm. Red lines correspond to fits based on equations S1 and S2 (see SI), respectively.

(A_t) in order to fit the obtained data. In fact, the absorption process has been shown to be prominent over scattering.[49]

By monitoring the absorbance evolution at λ = 203 nm over time (Figure 7b), a classical first order profile could be observed. In fact, the kinetic analysis was successfully carried out by fitting the obtained data by a pseudo-first order model (equation S1), leading to a rate constant of k_1 = 6.9×10^{-3} s^{-1} and R^2 values higher than 0.99. We now analyze the evolution of the extinction peak in the 225-260 nm region, which starts later and exhibits a more complex profile, as observed in Figure 7c (plotted for 248 nm). To describe the obtained profile, the data was fitted (R^2 higher than 0.99) with an equation based on the biologistic model of Meyer[50] that was recently reported to outline the growth of gold nanoparticles (Equation S2).[51] This model assumes two populational growth processes, in which the second starts before the first one is finished, at a different rate. Adapting this model to our results, we were able to identify an initial, slower, pseudo-first order reaction process (k_2 = 2.5×10^{-4} s^{-1}), followed by two different rate processes. From Equation S2, Δt_1 and Δt_2 are related to the duration of the respective formation stages, which corresponded to a slower process (185.9 s) and a faster one (15.5 s). In this sense, it is interesting to highlight that the two sigmoidal processes resemble a multi-step autocatalytic mechanism, in which a product acts as the catalyst for its own formation,[50] in accordance with our DFT results. For instance, these data could suggest that, in the beginning (pseudo-first order stage), the catalyst builds up until the required product is sufficient for the autocatalysis to happen in the next steps (sigmoidal stages). All kinetic parameters obtained from fitting with Equation S2 are given in Table S1.

Finally, based on the results discussed in this work, we may assume that the mechanism of NbS_2 oxidation follows a process that is similar to that observed for black phosphorus (BP) degradation.[52] Indeed, the chemisorption of O_2 (in the air or dissolved) on BP generates a more hydrophilic surface that catalyzes BP's degradation (oxidation). Here, we can speculate that O_2 is chemisorbed onto NbS_2 edges through exothermic and slow kinetic (k_1 *and* k_2) processes until NbSO is formed, as indicated by DFT, TGA, and kinetics analysis. After O_2 anchors onto NbS_2, further oxidation is facilitated, as suggested by DFT, and the autocatalytic processes begin, until reaching the final oxidation product which, according to our TGA and Raman results, would be a mixture of NbO_2 and Nb_2O_5. In fact, the extinction peak in the 225-260 nm region can tentatively be attributed to Nb_2O_5 formation, which has been reported to have strong absorption in the UV light region.[49] Besides, the broad range of this band could be a result of a mixture of different morphologies of the formed material or a mixture of Nb-oxides (including NbO_2).[53] It is important to mention that the band observed at around 278 nm (diamond in Figure 7a) could not be analyzed once the extinction (absolute value) actually drops with time. Thus, a kinetic fitting could not

be obtained in this case. Note that our current work considers NbS_2 flakes with a relatively narrow dispersion of lateral size and thickness. A thorough study as a function flake size and thickness would be elucidating but is beyond the scope of this work.

4. Summary and conclusions

In summary, we experimentally and theoretically investigated the NbS_2 stability under oxygen-rich environments. Structural, morphological and spectroscopical characterization of redox exfoliated NbS_2 flakes demonstrated different fingerprints regarding the oxidation mechanisms in both a solid (dried film over a substrate) and as a suspension (in acetonitrile) sample. Our theoretical analyses helped the elucidation of the mechanisms behind a most likely autocatalytic pathway for the oxygen-NbS_2 reaction. This process was in accordance with our kinetic study based on UV-Vis analysis. Finally, our theoretical Raman analysis was fundamental to identify new (and yet unknown) modes that emerged as a consequence of phase transition and oxidative processes. The proposed path of oxidation might be applied to different liquid-assisted exfoliation methods, since it is suggested that the material stability is closely related to its dimensions, instead of the method itself. Therefore, our study broadens the NbS_2 material understanding, which can contribute to its practical use in a range of 2D applications.

Author Contributions

D.A.N: conceptualization, methodology, experimental, writing – original draft. D.G: conceptualization, calculations, discussions, writing and reviewing. A.R.C: discussions, reviewing and editing. J.E.F: methodology, experimental, reviewing and editing. A.M.J: conceptualization, experimental, reviewing & editing. R.V: conceptualization, discussion, reviewing & editing. C.J.S.M: project supervisor, conceptualization, discussion, review & editing.

Conflicts of interest

There are no conflicts to declare.

5. Acknowledgments

All Brazilian authors acknowledge the financial support from FAPESP (Grant numbers: 2020/04374-6, 2020/13288-6, and 2018/25339-4), MackPesquisa, CNPq, CAPES, and the Brazilian Nanocarbon Institute of Science and Technology (INCT/Nanocarbono). DG acknowledge the financial support from FAPERJ (E-26/201.254/2022, E-26/210.296/2022, E-26/211.464/2021) and Instituto Serrapilheira (R-2012-37959) AMJ and RAV acknowledge the Air Force Office of Scientific Research (AFOSR) and the Air Force Research Laboratory's Materials and Manufacturing Directorate for their financial support.

References

1 X. Chia, A. Ambrosi, P. Lazar, Z. Sofer and M. Pumera, Electrocatalysis of layered Group 5 metallic transition metal dichalcogenides (MX2, M = V, Nb, and Ta; X = S, Se, and Te), *J Mater Chem A Mater*, 2016, **4**, 14241–14253.

2 S. A. Han, R. Bhatia and S. W. Kim, Synthesis, properties and potential applications of two-dimensional transition metal dichalcogenides, *Nano Converg*, , DOI:10.1186/s40580-015-0048-4.

3 M. Samadi, N. Sarikhani, M. Zirak, H. Zhang, H. L. Zhang and A. Z. Moshfegh, Group 6 transition metal dichalcogenide nanomaterials: Synthesis, applications and future perspectives, *Nanoscale Horiz*, 2018, **3**, 90–204.

4 Z. L. Liu, L. C. Cai and X. L. Zhang, Novel high pressure structures and superconductivity of niobium disulfide, *J Alloys Compd*, 2014, **610**, 472–477.

5 H. Bark, Y. Choi, J. Jung, J. H. Kim, H. Kwon, J. Lee, Z. Lee, J. H. Cho and C. Lee, Large-area niobium disulfide thin films as transparent electrodes for devices based on two-dimensional materials, *Nanoscale*, 2018, **10**, 1056–1062.

6 Y. Kim, K. C. Kwon, S. Kang, C. Kim, T. H. Kim, S. P. Hong, S. Y. Park, J. M. Suh, M. J. Choi, S. Han and H. W. Jang, Two-Dimensional NbS2 Gas Sensors for Selective and Reversible NO2 Detection at Room Temperature, *ACS Sens*, 2019, **4**, 2395–2402.

7 Y. Aray, D. Zambrano, M. H. Cornejo, E. v. Ludeña, P. Iza, A. B. Vidal, D. S. Coll, D. M. Jímenez, F. Henriquez and C. Paredes, First-principles study of the nature of niobium sulfide catalyst for hydrodesulfurization in hydrotreating conditions, *Journal of Physical Chemistry C*, 2014, **118**, 27823–27832.

8 D. Gopalakrishnan, A. Lee, N. K. Thangavel and L. M. Reddy Arava, Facile synthesis of electrocatalytically active NbS 2 nanoflakes for an enhanced hydrogen evolution reaction (HER), *Sustain Energy Fuels*, 2018, **2**, 96–102.

9 L. M. R. Arava, D. Gopalakrishnan and A. Lee, Electrocatalytically Active Niobium Sulfide Modified Carbon Cloth for Lithium-Sulfur Batteries, *Journal of Electrochemical Energy Conversion and Storage*, 2018, **15**, 1–5.

10 L. Najafi, S. Bellani, R. Oropesa-Nuñez, B. Martín-García, M. Prato, V. Mazánek, D. Debellis, S. Lauciello, R. Brescia, Z. Sofer and F. Bonaccorso, Niobium disulphide (NbS2)-based (heterogeneous) electrocatalysts for an efficient hydrogen evolution reaction, *J Mater Chem A Mater*, 2019, **7**, 25593–25608.

11 Y. Liu, J. Wu, K. P. Hackenberg, J. Zhang, Y. M. Wang, Y. Yang, K. Keyshar, J. Gu, T. Ogitsu, R. Vajtai, J. Lou, P. M. Ajayan, B. C. Wood and B. I. Yakobson, Self-optimizing, highly surface-active layered metal dichalcogenide catalysts for hydrogen evolution, *Nat Energy*, 2017, **2**, 1–7.

12 L. H. Hasimoto, J. Bettini, E. R. Leite, R. S. Lima, J. B. Souza Junior, L. Liu and M. Santhiago, Binary Cooperative Thermal Treatment of Cellulose and MoS 2 for the Preparation of Sustainable Paper-Based Electrochemical Devices for Hydrogen Evolution , *ACS Applied Engineering Materials*, , DOI:10.1021/acsaenm.2c00087.

13 X. Song, Y. Wang, F. Zhao, Q. Li, H. Q. Ta, M. H. Rümmeli, C. G. Tully, Z. Li, W. J. Yin, L. Yang, K. B. Lee, J. Yang, I. Bozkurt, S. Liu, W. Zhang and M. Chhowalla, Plasmon-Free Surface-Enhanced Raman Spectroscopy Using Metallic 2D Materials, *ACS Nano*, 2019, **13**, 8312–8319.

14 J. Yang, A. R. Mohmad, Y. Wang, R. Fullon, X. Song, F. Zhao, I. Bozkurt, M. Augustin, E. J. G. Santos, H. S. Shin, W. Zhang, D. Voiry, H. Y. Jeong and M. Chhowalla, Ultrahigh-current-density niobium disulfide catalysts for hydrogen evolution, *Nat Mater*, 2019, **18**, 1309–1314.

15 A. Jawaid, J. Che, L. F. Drummy, J. Bultman, A. Waite, M. S. Hsiao and R. A. Vaia, Redox Exfoliation of Layered Transition Metal Dichalcogenides, *ACS Nano*, 2017, **11**, 635–646.

16 M. Nyman, Polyoxoniobate chemistry in the 21st century, *Dalton Transactions*, 2011, **40**, 8049–8058.

17 M. Maldonado, M. L. da Silva Neto, P. G. Vianna, H. B. Ribeiro, C. B. de Araújo, C. J. S. D. Matos, L. Seixas, A. M. Jawaid, R. Busch, A. J. Ritter, R. A. Vaia and A. S. L. Gomes, Femtosecond nonlinear refraction of 2D semi-metallic redox exfoliated ZrTe2at 800 nm, *Appl Phys Lett*, , DOI:10.1063/5.0031649.

18 A. M. Jawaid, A. J. Ritter and R. A. Vaia, Mechanism for Redox Exfoliation of Layered Transition Metal Dichalcogenides, *Chemistry of Materials*, 2020, **32**, 6550–6565.

19 M. E. Maldonado, A. Das, A. M. Jawaid, A. J. Ritter, R. A. Vaia, D. A. Nagaoka, P. G. Vianna, L. Seixas, C. J. S. de Matos, A. Baev, P. N. Prasad and A. S. L. Gomes, Nonlinear Optical Interactions and Relaxation in 2D Layered Transition Metal Dichalcogenides Probed by

Optical and Photoacoustic Z-Scan Methods, *ACS Photonics*, 2020, **7**, 3440–3447.

20 K. Kalantar-zadeh, J. Z. Ou, T. Daeneke, A. Mitchell, T. Sasaki and M. S. Fuhrer, Two dimensional and layered transition metal oxides, *Appl Mater Today*, 2016, **5**, 73–89.

21 A. Jawaid, N. A. Pike, R. Pachter and R. Vaia, Basal Surface Hybridization of Group v Layered Transition Metal Dichalcogenides, *ACS Materials Au*, , DOI:10.1021/acsmaterialsau.2c00049.

22 C. H. Chu and C. W. Leung, The convolution equation of Choquet and Deny on [IN]-groups, *Integral Equations and Operator Theory*, 2001, **40**, 391–402.

23 P. Giannozzi, O. Andreussi, T. Brumme, O. Bunau, M. Buongiorno Nardelli, M. Calandra, R. Car, C. Cavazzoni, D. Ceresoli, M. Cococcioni, N. Colonna, I. Carnimeo, A. Dal Corso, S. de Gironcoli, P. Delugas, R. A. Distasio, A. Ferretti, A. Floris, G. Fratesi, G. Fugallo, R. Gebauer, U. Gerstmann, F. Giustino, T. Gorni, J. Jia, M. Kawamura, H. Y. Ko, A. Kokalj, E. Kücükbenli, M. Lazzeri, M. Marsili, N. Marzari, F. Mauri, N. L. Nguyen, H. v. Nguyen, A. Otero-De-La-Roza, L. Paulatto, S. Poncé, D. Rocca, R. Sabatini, B. Santra, M. Schlipf, A. P. Seitsonen, A. Smogunov, I. Timrov, T. Thonhauser, P. Umari, N. Vast, X. Wu and S. Baroni, Advanced capabilities for materials modelling with Quantum ESPRESSO, *Journal of Physics Condensed Matter*, , DOI:10.1088/1361-648X/aa8f79.

24 P. Giannozzi, S. Baroni, N. Bonini, M. Calandra, R. Car, C. Cavazzoni, D. Ceresoli, G. L. Chiarotti, M. Cococcioni, I. Dabo, A. Dal Corso, S. de Gironcoli, S. Fabris, G. Fratesi, R. Gebauer, U. Gerstmann, C. Gougoussis, A. Kokalj, M. Lazzeri, L. Martin-Samos, N. Marzari, F. Mauri, R. Mazzarello, S. Paolini, A. Pasquarello, L. Paulatto, C. Sbraccia, S. Scandolo, G. Sclauzero, A. P. Seitsonen, A. Smogunov, P. Umari and R. M. Wentzcovitch, QUANTUM ESPRESSO: A modular and open-source software project for quantum simulations of materials, *Journal of Physics Condensed Matter*, , DOI:10.1088/0953-8984/21/39/395502.

25 G. Prandini, A. Marrazzo, I. E. Castelli, N. Mounet and N. Marzari, Precision and efficiency in solid-state pseudopotential calculations, *NPJ Comput Mater*, , DOI:10.1038/s41524-018-0127-2.

26 M. Lazzeri and F. Mauri, First-Principles Calculation of Vibrational Raman Spectra in Large Systems: Signature of Small Rings in Crystalline [Formula presented], *Phys Rev Lett*, 2003, **90**, 4.

27 C. Backes, T. M. Higgins, A. Kelly, C. Boland, A. Harvey, D. Hanlon and J. N. Coleman, Guidelines for exfoliation, characterization and processing of layered materials produced by liquid exfoliation, *Chemistry of Materials*, 2017, **29**, 243–255.

28 C. Backes, R. J. Smith, N. McEvoy, N. C. Berner, D. McCloskey, H. C. Nerl, A. O'Neill, P. J. King, T. Higgins, D. Hanlon, N. Scheuschner, J. Maultzsch, L. Houben, G. S. Duesberg, J. F. Donegan, V. Nicolosi and J. N. Coleman, Edge and confinement effects allow in situ measurement of size and thickness of liquid-exfoliated nanosheets, *Nat Commun*, 2014, **5**, 1–10.

29 C. Sourisseau, R. Cavagnat and J. L. Tirado, A Raman study of the misfit layer compounds, (SnS)1.17NbS2 and (PbS)1.18 TiS2, *Journal of Raman Spectroscopy*, 1992, **23**, 647–651.

30 S. Nakashima, Y. Tokuda, A. Mitsuishi, R. Aoki and Y. Hamaue, Raman scattering from 2H-NbS2 and intercalated NbS2, *Solid State Commun*, 1982, **42**, 601–604.

31 S. Zhao, T. Hotta, T. Koretsune, K. Watanabe, T. Taniguchi, K. Sugawara, T. Takahashi, H. Shinohara and R. Kitaura, Two-dimensional

metallic NbS2: Growth, optical identification and transport properties, *2d Mater*, 2016, **3**, 1–9.

32 A. Kozhakhmetov, T. H. Choudhury, Z. Y. al Balushi, M. Chubarov and J. M. Redwing, Effect of substrate on the growth and properties of thin 3R NbS2 films grown by chemical vapor deposition, *J Cryst Growth*, 2018, **486**, 137–141.

33 W. Ge, K. Kawahara, M. Tsuji and H. Ago, Large-scale synthesis of NbS2 nanosheets with controlled orientation on graphene by ambient pressure CVD, *Nanoscale*, 2013, **5**, 5773–5778.

34 X. Wang, J. Lin, Y. Zhu, C. Luo, K. Suenaga, C. Cai and L. Xie, Chemical vapor deposition of trigonal prismatic NbS2 monolayers and 3R-polytype few-layers, *Nanoscale*, 2017, **9**, 16607–16611.

35 Y. Chen, Z. Lai, X. Zhang, Z. Fan, Q. He, C. Tan and H. Zhang, Phase engineering of nanomaterials, *Nat Rev Chem*, 2020, **4**, 243–256.

36 C. Witteveen, K. Górnicka, J. Chang, M. Månsson, T. Klimczuk and F. O. von Rohr, Polytypism and superconductivity in the NbS2system, *Dalton Transactions*, 2021, **50**, 3216–3223.

37 C. Huang, W. Dong, C. Dong, X. Wang, B. Jia and F. Huang, Niobium dioxide prepared by a novel La-reduced route as a promising catalyst support for Pd towards the oxygen reduction reaction, *Dalton Transactions*, 2020, **49**, 1398–1402.

38 M. P. F. Graça, A. Meireles, C. Nico and M. A. Valente, Nb2O5 nanosize powders prepared by sol-gel-Structure, morphology and dielectric properties, *J Alloys Compd*, 2013, **553**, 177–182.

39 Y. Zhao, Z. Zhang and Y. Lin, Optical and dielectric properties of a nanostructured NbO2 thin film prepared by thermal oxidation, *J Phys D Appl Phys*, 2004, **37**, 3392–3395.

40 E. S. Lyle, C. McAllister, D. C. Dahn and R. Bissessur, Exfoliated MoS2–Polyaniline Nanocomposites: Synthesis and Characterization, *J Inorg Organomet Polym Mater*, 2020, **30**, 206–213.

41 K. Izawa, S. Ida, U. Unal, T. Yamaguchi, J. H. Kang, J. H. Choy and Y. Matsumoto, A new approach for the synthesis of layered niobium sulfide and restacking route of NbS2 nanosheet, *J Solid State Chem*, 2008, **181**, 319–324.

42 R. Tenne, C. Schuffenhauer and G. Wildermuth, ¨ rgen Felsche*, 2004, 3991–4002.

43 W. Zhang, S. Ning, S. Zhang, S. Wang, J. Zhou, X. Wang and Y. Wei, Synthesis of functional silica composite resin for the selective separation of zirconium from scandium, *Microporous and Mesoporous Materials*, 2019, **288**, 109602.

44 O. F. O. Of and A. Tatsuki, Results and discussion Thermal analysis of NbS2, 1986, **32**, 1105–1113.

45 Y. Liao, K. S. Park, P. Singh, W. Li and J. B. Goodenough, Reinvestigation of the electrochemical lithium intercalation in 2H- and 3R-NbS2, *J Power Sources*, 2014, **245**, 27–32.

46 L. Li, L. Pang, Q. Zhao, Y. Wang and W. Liu, Niobium disulfide as a new saturable absorber for an ultrafast fiber laser, *Nanoscale*, 2020, **12**, 4537–4543.

47 X. Sun, B. Shi, H. Wang, N. Lin, S. Liu, K. Yang, B. Zhang and J. He, Optical Properties of 2D 3R Phase Niobium Disulfide and Its Applications as a Saturable Absorber, *Adv Opt Mater*, 2020, **8**, 1–11.

48 A. Fakih, O. Shinde, J. Biscaras and A. Shukla, Raman evidence for absence of phase transitions in negative differential resistance thin film devices of niobium dioxide, *J Appl Phys*, , DOI:10.1063/1.5140543.

49 J. Wu, J. Wang, H. Li, Y. Du, X. Jia and B. Liu, New fluorine-doped H2(H2O)Nb2O6photocatalyst for the degradation of organic dyes, *CrystEngComm*, 2014, **16**, 9675–9684.

50 P. S. Meyer, J. W. Yung and J. H. Ausubel, A Primer on Logistic Growth and Substitution: The Mathematics of the Loglet Lab Software, *Technol Forecast Soc Change*, 1999, **61**, 247–271.

51 I. Rocha, E. Lucht, I. C. Riegel-Vidotti, M. Vidotti and E. S. Orth, Kinetic Approach to Elucidate Size Controllable Features in Nanocomposites of Gold Nanoparticles and Poly(3,4-ethylenedioxythiophene) in Aqueous Dispersion Stabilized by Gum Acacia, *The Journal of Physical Chemistry C*, 2014, **118**, 25756–25764.

52 Y. Huang, J. Qiao, K. He, S. Bliznakov, E. Sutter, X. Chen, D. Luo, F. Meng, D. Su, J. Decker, W. Ji, R. S. Ruoff and P. Sutter, Interaction of black phosphorus with oxygen and water, *Chemistry of Materials*, 2016, **28**, 8330–8339.

53 K. Arshak, G. Hickey, J. Harris and E. Forde, Ozone sensing properties of NbO2 thin films for health and safety applications, *2008 IEEE Sensors Applications Symposium, SAS-2008 - Proceedings*, 2008, 187–192.